

A deep look at the nuclear region of UGC 5101 through high angular resolution mid-IR data with GTC/CanariCam

M. Martínez-Paredes,^{1★} A. Alonso-Herrero,^{2†} I. Aretxaga,¹ C. Ramos Almeida,^{3,4‡}
A. Hernán-Caballero,² O. González-Martín,^{3,4,5} M. Pereira-Santaella,⁶ C. Packham,⁷
A. Asensio Ramos,^{3,4} T. Díaz-Santos,^{8,9} M. Elitzur,^{10,11} P. Esquej,¹²
I. García-Bernete,^{3,4} M. Imanishi,^{13,14,15} N. A. Levenson¹⁶
and J. M. Rodríguez Espinosa^{3,4}

¹Instituto Nacional de Astrofísica, Óptica y Electrónica (INAOE), Luis Enrique Erro 1, Sta. Ma. C.P. 72840 Tonantzintla, Puebla, Mexico

²Instituto de Física de Cantabria, CSIC-UC, E-39005 Santander, Spain

³Instituto de Astrofísica de Canarias (IAC), E-38205 La Laguna, Tenerife, Spain

⁴Departamento de Astrofísica, Universidad de la Laguna (ULL), E-38206 La Laguna, Tenerife, Spain

⁵Centro de Radioastronomía y Astrofísica UNAM, Apartado Postal 3-72 (Xangari), 58089 Morelia, Michoacán, Mexico

⁶Centro de Astrobiología, CSIC-INTA, E-28850 Torrejón de Ardoz, Madrid, Spain

⁷Department of Physics and Astronomy, University of Texas at San Antonio, San Antonio, TX 78249, USA

⁸Spitzer Science Center, California Institute of Technology, MS 220-6, Pasadena, CA 91125, USA

⁹Núcleo de Astronomía de la Facultad de Ingeniería, Universidad Diego Portales, Av. Ejército Libertador 441, Santiago, Chile

¹⁰Astronomy Department, University of California, Berkeley, CA 94720-3411, USA

¹¹Physics and Astronomy, University of Kentucky, Lexington, KY 40506-0055, USA

¹²Departamento de Astrofísica, Universidad Complutense de Madrid, E-28040 Madrid, Spain

¹³Subaru Telescope, 650 North A'ohoku Place, Hilo, HI 96720, USA

¹⁴National Astronomical Observatory of Japan, 2-21-1 Osawa, Mitaka, Tokyo 181-8588, Japan

¹⁵Department of Astronomical Science, The Graduate University for Advanced Studies (SOKENDAI), 2-21-1 Osawa, Mitaka, Tokyo 181-8588, Japan

¹⁶Gemini Observatory, Casilla 603, La Serena, Chile

Accepted 2015 September 14. Received 2015 September 4; in original form 2015 February 3

ABSTRACT

We present an analysis of the nuclear infrared (IR, 1.6–18 μm) emission of the ultraluminous IR galaxy UGC 5101 to derive the properties of its active galactic nucleus (AGN) and its obscuring material. We use new mid-IR high angular resolution (0.3–0.5 arcsec) imaging using the Si-2 filter ($\lambda_C = 8.7 \mu\text{m}$) and 7.5–13 μm spectroscopy taken with CanariCam (CC) on the 10.4 m Gran Telescopio CANARIAS. We also use archival *Hubble Space Telescope*/NICMOS and Subaru/COMICS imaging and *Spitzer*/IRS spectroscopy. We estimate the near- and mid-IR unresolved nuclear emission by modelling the imaging data with GALFIT. We decompose the *Spitzer*/IRS and CC spectra using a power-law component, which represents the emission due to dust heated by the AGN, and a starburst component, both affected by foreground extinction. We model the resulting unresolved near- and mid-IR, and the starburst subtracted CC spectrum with the CLUMPY torus models of Nenkova et al. The derived geometrical properties of the torus, including the large covering factor and the high foreground extinction needed to reproduce the deep 9.7 μm silicate feature, are consistent with the lack of strong AGN signatures in the optical. We derive an AGN bolometric luminosity $L_{\text{bol}} \sim 1.9 \times 10^{45} \text{ erg s}^{-1}$ that is in good agreement with other estimates in the literature.

Key words: galaxies: active – galaxies: individual: UGC 5101 – galaxies: Seyfert – infrared: galaxies.

1 INTRODUCTION

Ultraluminous infrared galaxies (ULIRGs) are among the most luminous objects in the local universe, with both their luminosities ($L_{\text{IR}} > 10^{12} L_{\odot}$ emerging mainly in the far-infrared) and space densities being similar to those of quasars (e.g. Sanders & Mirabel

* E-mail: mariela@inaoe.mx

† Visiting Professor, Department of Physics, Astronomy, University of Texas at San Antonio.

‡ Marie Curie Fellow.

1996). ULIRGs have large molecular gas concentrations in their central kpc regions (e.g. Downes & Solomon 1998) with densities comparable to those of the stars of elliptical galaxies. For increasing infrared (IR) luminosities, their mid-IR slopes and silicate depths also increase, suggesting that their nuclei are more obscured and more compact (Stierwalt et al. 2013 and references therein). Kormendy & Sanders (1992) proposed that ULIRGs evolve into elliptical galaxies through merger-induced dissipative collapse. In this scenario, these mergers first go through a luminous starburst phase, followed by a dust-enshrouded active galactic nucleus (AGN) phase, and finally evolve into an optically bright, *naked* quasar once they either consume or shed their shells of gas and dust (Sanders et al. 1988a).

The target of interest in this paper is the nearby ($z = 0.039$; Kim 1995) ULIRG UGC 5101 (IRAS 09320+6134) with a luminosity distance $d = 168$ Mpc (1 arcsec = 755 pc) for $H_0 = 73$ km s⁻¹ Mpc⁻¹, $\Omega_M = 0.27$, $\Omega_\Lambda = 0.73$, and an IR luminosity $L_{\text{IR}} = 10^{12} L_\odot$ (Sanders et al. 1988a). In the optical and near-IR the galaxy has a single, very red nucleus within a disturbed morphology, suggestive of a recent interaction and merger (Sanders et al. 1988b; Scoville et al. 2000; Surace, Sanders & Evans 2000).

Optically the AGN has been classified as a Seyfert 1.5 (Sanders et al. 1988a), a LINER (Veilleux et al. 1995), and a Seyfert 2 (Yuan, Kewley & Sanders 2010). Mid-IR spectroscopy taken with *ISO* (Genzel et al. 1998) as well as ground-based *L*-band spectroscopy (Imanishi, Dudley & Maloney 2001) demonstrated the presence of a powerful nuclear starburst. Using ground-based high angular resolution mid-IR imaging, Soifer et al. (2000) showed that ~ 60 per cent of the *IRAS* flux at 12 μm comes from the central 4 arcsec (~ 3 kpc) and that almost half of this arises in an unresolved core. Based on its *IRAS* colours, UGC 5101 is classified as a cold, starburst-dominated, far-IR source. However, *Chandra* and *XMM-Newton* data detected the Fe-K α line, which together with the low observed $L_{2-10\text{keV}}/L_{\text{IR}}$ and $L_{2-10\text{keV}}/L_{[\text{O III}]}$ ratios likely indicate the presence of a Compton-thick AGN (Imanishi et al. 2003; Ptak et al. 2003; González-Martín et al. 2009). At radio wavelengths, the nucleus of UGC 5101 has a high brightness temperature ($T > 10^7$ K) with a morphology resembling that of a jet, again pointing to the presence of an AGN (Lonsdale, Smith & Lonsdale 1995; Lonsdale et al. 2003). Using *Spitzer* IR spectrograph (IRS; Houck et al. 2004) data, Armus et al. (2004, 2007) detected the mid-IR fine structure line of [Ne v] at 14.3 μm , which confirms the presence of an AGN in the nucleus of this galaxy.

UGC 5101 offers an ideal scenario for studying the interplay between nuclear activity and star formation in a nearby ULIRG. The ~ 5 –10 arcsec spatial resolution of *Spitzer*/IRS only allowed us to study this interplay in ULIRGs on kpc-scales, although with extremely good sensitivity. For instance, Veilleux et al. (2009) used different indicators on the *Spitzer*/IRS spectrum of this galaxy and estimated an average IR luminosity, whereas Armus et al. (2007) estimated a 30 per cent contribution from a starburst component.

Here, we present new high spatial resolution (~ 0.3 arcsec ~ 230 pc) mid-IR imaging and spectroscopy of UGC 5101 obtained with CanariCam (CC; Telesco et al. 2003; Packham et al. 2005) on the 10.4 m Gran Telescopio CANARIAS (GTC). We use these observations to disentangle the unresolved mid-IR emission, which is presumably due to dust heated by the AGN, from that due to star formation in the nuclear region of the host galaxy. By modelling the unresolved near-IR and mid-IR emission with the CLUMPY torus models of Nenkova et al. (2008a,b), we aim to derive the physical and geometrical properties of the obscuring material surrounding the AGN of UGC 5101. The paper is organized as follows.

Section 2 presents the observations and data reduction. In Section 3, we estimate the unresolved emission in the near-IR and mid-IR using the imaging and spectroscopic data. In Section 4, we model the unresolved near and mid-IR emission of UGC 5101 and derive the properties of the AGN and its obscuring material. Section 5 gives the conclusions of this work.

2 OBSERVATIONS AND DATA REDUCTION

2.1 GTC/CC mid-IR imaging and spectroscopy

As part of an ESO/GTC large programme (ID: 182.B-2005, PI: A. Alonso-Herrero) to observe a large sample of local AGN, in 2014 January 6, we observed in queue mode UGC 5101 with CC on the GTC in El Roque de los Muchachos Observatory (La Palma, Spain). CC uses a Raytheon 320 \times 240 Si:As detector that covers a field of view (FOV) of 26 arcsec \times 19 arcsec on the sky with a plate scale of 0.0798 arcsec pixel⁻¹. We obtained an imaging observation with the Si-2 filter ($\lambda_c = 8.7$ μm and width $\Delta\lambda_{\text{cut}} = 1.1$ μm at 50 per cent cut-on/off) using the standard mid-IR chop-nod technique. The chop and nod throws were 15 arcsec. The air-mass during the observation was ~ 1.2 . We observed the mid-IR spectrophotometric standard star HD 79354 (Cohen 1999) before the science target. Allowing for overheads, this was 20 min before the science observations. The standard star is used to perform the photometric calibration, estimate the full width half-maximum (FWHM) of the science observation, and perform the point spread function (PSF) subtraction. We measured the FWHM of the data by fitting the radial profile of the standard star with a Gaussian function and obtained a value of 0.4 arcsec. Table 1 summarizes the details of the observations.

We also obtained long-slit mid-IR spectroscopy of the nuclear region of UGC 5101 on the same night. We used the low spectral resolution 10 μm grating, which covers the *N*-band ~ 7.5 –13 μm with a nominal spectral resolution of $R = \lambda/\Delta\lambda \sim 175$, and a 0.52 arcsec width slit. In Table 1, we list the position angles (PA) of the slit, measured from the north to the east. The observing sequence was as follows. We first took an acquisition image of the galaxy with the Si-2 filter, then centred the slit on the peak mid-IR brightness, and finally integrated for the on-source integration times given in Table 1. We used the same chop-nod parameters as for the imaging observations. We also observed standard stars using the same observing sequence to provide the photometric calibration, the telluric correction, and the slit loss correction. We also used the acquisition image of the standard star to obtain the FWHM of the spectroscopic observation (see Table 1).

Table 1. Summary of the GTC/CC observations.

UGC 5101	Imaging	Spectroscopy
Date	2014.01.06	2014.01.06
$N_{\text{OB}} \times t_{\text{on}}$ (s)	1 \times 1224	1 \times 1242
Standard	HD 79354	HD 79354
$N_{\text{OB}} \times t_{\text{on-STD}}$ (s)	1 \times 60	1 \times 60
FWHM (arcsec)	0.4	0.3
PA ($^\circ$)	0	90

Notes. N_{OB} is the number of repetitions performed, t_{on} is the on-source integration time of UGC 5101 and $t_{\text{on-STD}}$ is the on-source integration time of the standard star. The FWHM is measured from the image of the standard star. The PA value for imaging is the orientation of the detector on the sky, while for spectroscopy it indicates the orientation of the slit.

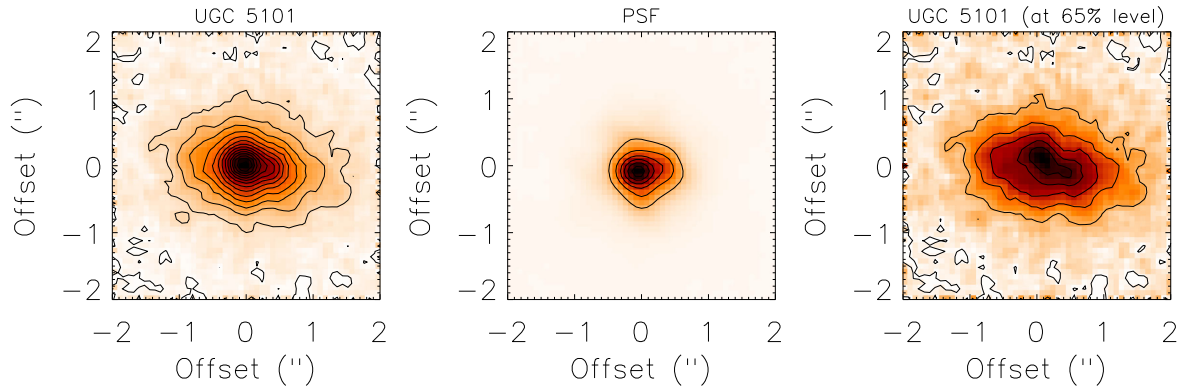


Figure 1. The left-hand panel is the fully reduced GTC/CC 8.7 μm (Si-2 filter) image of UGC 5101, in the middle is the PSF standard star shown in a linear scale. The right-hand panel is the PSF-scaled (at the 65 per cent peak level, see Section 3.1.2) subtracted image of UGC 5101. The lowest contour is 3σ over the background, with the next contours in 2σ steps (except in the PSF image). The orientation of all the images is north up, east to the left. The physical scale of the UGC 5101 images is $755 \text{ pc arcsec}^{-1}$.

We reduced the CC data using the REDCAN pipeline for the reduction and analysis of ground-based mid-IR CC and T-ReCS imaging and spectroscopic data (González-Martín et al. 2013). Briefly, the reduction process of the imaging data includes sky subtraction, stacking of the individual images, and rejection of bad images. The flux calibration of the galaxy image is done using the observation of the standard star. Fig. 1 (left-hand panel) shows the fully reduced 8.7 μm CC image of UGC 5101 together with that of the standard star (middle panel). As also found by Soifer et al. (2000) at 12 μm using the Keck telescope, UGC 5101 is clearly extended in the mid-IR (see Section 3.2).

For the spectroscopy, the first three steps of the data reduction are the same as for the imaging. Additionally, REDCAN performs the two-dimensional wavelength calibration of the target and standard star spectra using sky lines. Then, the trace determination is made using the observation of the standard star. The last steps of the data reduction include the extraction of the spectra either as point sources or extended sources and finally, the correction for slit losses in the case of point source extractions.

2.2 Archival *HST*/NICMOS and Subaru/COMICS imaging

Our target was observed in a single orbit in 1997 November 7 with the *Hubble Space Telescope* (*HST*) using camera 2 of NICMOS (Thompson et al. 1998) as part of the Guaranteed Time Observations. This camera uses a 256×256 HgCdTe array with pixel scales of 0.0762 arcsec and $0.0755 \text{ arcsec pixel}^{-1}$ in x and y , respectively, providing a $\sim 19.5 \text{ arcsec} \times 19.3 \text{ arcsec}$ FOV. We use the images of UGC 5101 taken with the broad-band *F160W* filter ($\lambda_c = 1.60 \mu\text{m}$) and the medium-band *F222M* filter ($\lambda_c = 2.22 \mu\text{m}$). We downloaded the five reduced and calibrated images in each of the *F160W* and *F222M* filters from the Mikulski Archive for Space Telescopes (MAST). We combined the individual exposures of each filter using the average of the images. These images were originally presented and analysed in Scoville et al. (2000).

We also downloaded a fully reduced and calibrated image of UGC 5101 taken in the *Q*-band ($\lambda_c = 17.7 \mu\text{m}$) from the German Virtual Observatory (GAVO) hosted at the Virtual Observatory (VO). The image was obtained with COMICS on the Subaru Telescope in Mauna Kea, Hawaii. It has an FOV and a pixel scale of $42 \text{ arcsec} \times 32 \text{ arcsec}$ and $0.13 \text{ arcsec pixel}^{-1}$, respectively. For full details on the *Q*-band observations and data reduction, we refer the reader to Asmus et al. (2014).

2.3 *Spitzer*/IRS spectroscopy

UGC 5101 was observed with *Spitzer*/IRS using the short-low (SL) and long-low (LL) modules covering the following spectral ranges: SL1; 7.4–14.5 μm , SL2; 5.2–7.7 μm , LL1; and 19.5–38.0 μm , LL2; 14.0–21.3 μm , with a spectral resolution of $R \sim 60$ –120. The SL slit width is 3.7 arcsec, whereas that of the LL module is 10.5 arcsec. We downloaded the fully calibrated staring mode spectrum from the Cornell Atlas of *Spitzer*/IRS Source (CASSIS v6; Lebouteiller et al. 2011). CASSIS has identified this object as point-like and therefore it uses its *optimal extraction* routine to produce the best flux-calibrated spectrum and ensure the best S/N ratio. We stitched the different module spectra together by using the shortest module SL2 flux as reference spectrum for the other modules. The scaling factors were 1.1 for LL1 and LL2.

3 ANALYSIS

3.1 Unresolved nuclear emission from the imaging data

Even at high spatial resolutions, in the near-IR up to $\lambda \sim 2 \mu\text{m}$, extended stellar emission arising in the host galaxy contaminates and even dominates the nuclear fluxes of AGN, especially in type 2s. At longer wavelengths $\lambda > 3 \mu\text{m}$ contamination by stellar photospheric emission is greatly reduced (Alonso-Herrero et al. 2001 and references therein). Our goal in this section is to use the high angular resolution imaging data to isolate as much as possible the unresolved nuclear emission before we attempt to infer the properties of the obscuring material and the AGN luminosity of UGC 5101 (Section 4). To do so, we need to remove any extended nuclear emission not directly related to the dusty torus and/or emission arising from dust heated by young massive stars (see Alonso-Herrero et al. 2011 and references therein).

Although in the past there have been some attempts to measure the unresolved nuclear emission of UGC 5101 at near- and mid-IR wavelengths (e.g. Scoville et al. 2000; Soifer et al. 2000; Haan et al. 2011; Asmus et al. 2014; Imanishi & Saito 2014), the reported values may still be contaminated by stellar emission and emission due to nuclear star formation. Therefore, we measure the unresolved emission consistently in the archival *HST*/NICMOS *H*- and *K*-band images and COMICS *Q*-band images as well as in the new CC image. To do so, we use the two-dimensional fitting algorithm GALFIT (Peng et al. 2002) to derive both the unresolved nuclear emission

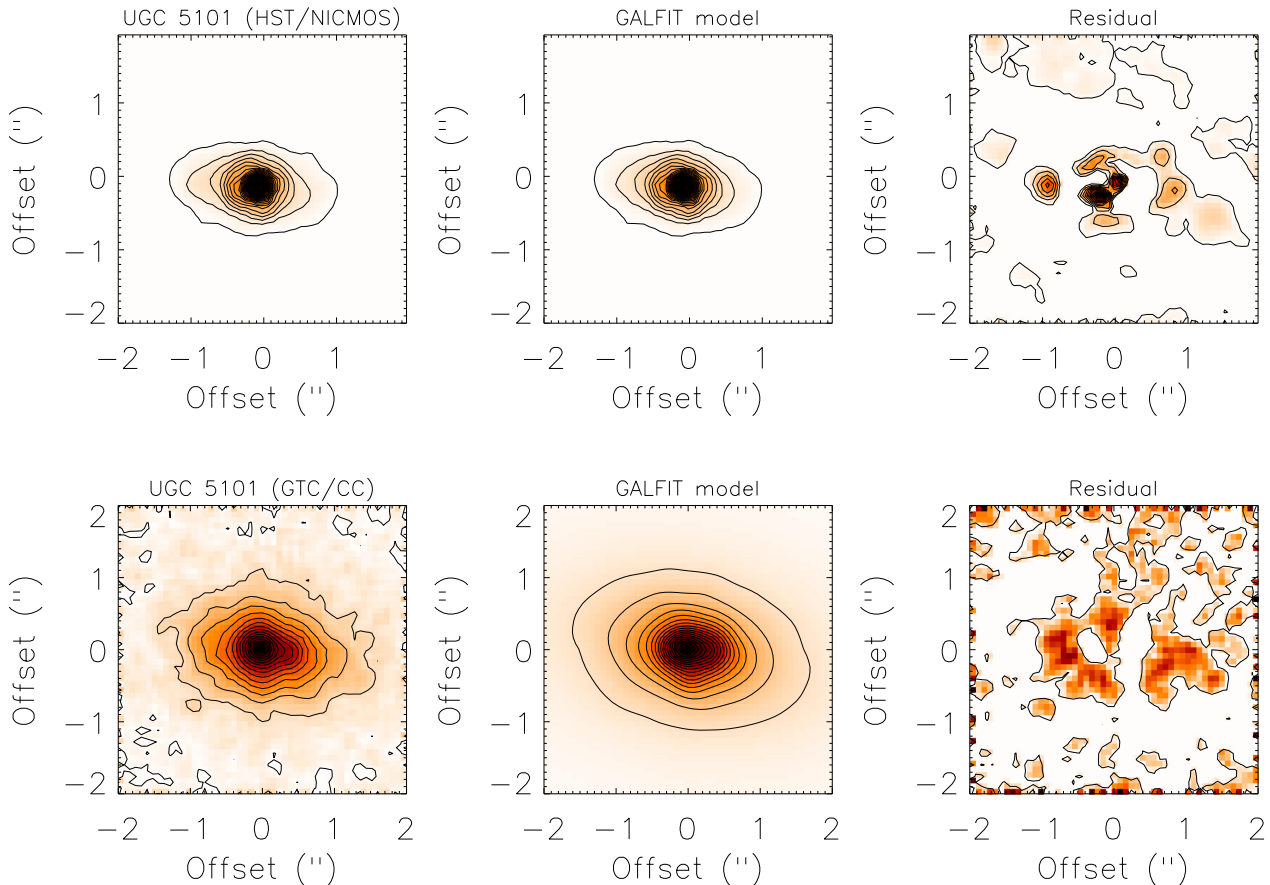


Figure 2. Upper panels: to the left is the combined *HST*/NICMOS 2.22 μm image (*F222M* filter) of the nuclear region of UGC 5101, in the middle the GALFIT model image (see Table 2 for the parameters), and to the right the residual image after subtracting the GALFIT model from the original image. The images are shown in a linear scale, rotated so that north is up, east is to the left. The lowest contour is 3σ above the background, with the next contours in 2σ steps. Lower panels: same as upper panels but for the reduced GTC/CC 8.7 μm (Si-2 filter) image. The physical scale of the images is $755 \text{ pc arcsec}^{-1}$.

and extended emission, as GALFIT allows us to simultaneously fit an arbitrary number of components (e.g. PSF, Sérsic profile, exponential disc, and/or Gaussian functions) to a galaxy image. It is possible, however, that even at these high angular resolutions (0.15–0.40 arcsec) there is still some contamination from other components (stellar emission and star formation, see Section 4).

3.1.1 Near-IR emission

To model the unresolved nuclear emission, we generated theoretical Tiny Tim PSFs for the NICMOS camera 2 *F160W4* and *F222M* filters. The Tiny Tim (Krist 1993) PSFs have only three free parameters, namely the central coordinates (x_c and y_c) and the total flux. The total unresolved emission is computed by integrating the flux over the PSF image assuming that it contains 100 per cent of the light. To fit the extended surface brightness distribution, that is, the host galaxy emission, we used a Sérsic profile (see Peng et al. 2002 for more details on profiles).

To constrain the unresolved emission in the near-IR and its uncertainty, we use different combinations of profiles that always include a PSF profile to represent the unresolved emission. These combinations of profiles are: a PSF and a Sérsic profile with all the parameters free, a PSF plus a Sérsic profile with fixed $n = 1$, a PSF plus a Sérsic profile with fixed $n = 4$, and finally one PSF plus two

Sérsic profiles including a Gaussian profile¹ with all the parameters left to vary freely. We find that the models that include a PSF plus two Sérsic profiles with free parameters and a PSF plus one Sérsic profile with $n = 4$ produce fits with similar $\chi^2 \sim 0.35$ and that the unresolved emission measured on the NICMOS images did not change by more than 1 per cent at both wavelengths. We then conclude that the unresolved component is well constrained at both near-IR wavelengths. Fig. 2 shows the combined NICMOS 2.22 μm image together with the GALFIT model image and the residual image after subtracting the GALFIT model from the image.

Since the fits with different models are of similar quality, we estimate the uncertainty of the parameters in Table 2 as the standard deviation of the values given by all models. These uncertainties are larger than those estimated for a single model.

The unresolved emission detected in UGC 5101 contributes 2 and 17 per cent of the continuum emission at 1.60 and 2.22 μm , respectively, measured over the *HST*/NICMOS Camera 2 FOV. Our unresolved fluxes at *H* and *K* band are lower than those reported by Scoville et al. (2000) using the same NICMOS/*HST* images. This is because they only subtracted the underlying galaxy as estimated from the adjacent pixels instead of modelling the host galaxy emission. The *H*-band image was also analysed by Haan et al. (2011)

¹ A Gaussian profile is a special case of the Sérsic profile when $n = 0.5$ and the size parameter is the FWHM instead of r_{eff} .

Table 2. Results from the GALFIT modelling using a PSF + Sérsic profile model.

Instrument	λ (μm)	f_{unresol} (mJy)	$f_{\text{Sérsic}}$ (mJy)	n	r_{eff} (pc)	a/b	PA ($^\circ$)
NICMOS	1.60	<1.3	21 ± 6	4*	1753 ± 728	0.60 ± 0.03	82 ± 2
NICMOS	2.22	5 ± 2	25 ± 6	4*	1091 ± 584	0.60 ± 0.03	82 ± 3
CC	8.70	36 ± 4	169 ± 10	2.0 ± 0.2	1127 ± 65	0.60 ± 0.02	78 ± 1

Notes. Column 1: instrument. Column 2: central wavelength of the filter. Column 3: unresolved nuclear emission. Column 4: emission of the Sérsic component. Column 5: index of the Sérsic profile. *For the 1.60 and 2.22 μm model the index was fixed. Column 6: effective radius in pc of the Sérsic component. Column 7: axis ratio of the Sérsic component. Column 8: PA of the major axis of the Sérsic component measured east of north.

using a similar decomposition technique as used here, where they found similar results for PSF contribution and Sérsic parameters, within the uncertainties. We adopt our own values for the analysis that follows, since our estimation of PSF uncertainties follows the same methodology as that used to measure the unresolved component at K and mid-IR bands, and it considers a larger range of models than in the analysis by Haan et al. The host galaxy parameters are similar to those found in previous studies at both near-IR bands (e.g. Scoville et al. 2000; Haan et al. 2011; Medling et al. 2014).

3.1.2 Mid-IR emission

As done for the *HST*/NICMOS images, we also run GALFIT on the CC 8.7 μm image to estimate the unresolved and integrated emission of the galaxy. For the unresolved component, we used the CC observation of the standard star taken just before the galaxy observation. We assume that the FWHM did not vary on those time-scales and therefore the emission of the standard star can be used to represent the unresolved emission of UGC 5101. We fit a PSF and Sérsic component with all parameters left free to vary. The best fit had a reduced $\chi^2 \sim 1$. The uncertainties for the parameters are the standard deviation of the parameters derived by considering different convolution boxes. The lower panels of Fig. 2 show the original CC 8.7 μm image together with the 2D GALFIT model and the residual image. After subtracting the GALFIT model, we obtained a residual of less than 1.5 per cent when compared to the flux in the original image. Table 3 lists the unresolved and Sérsic fluxes at 8.7 μm . The unresolved component contributes ~ 12 per cent of the observed emission at this wavelength. The uncertainties in the reported profile fluxes are the formal photometric errors reported by GALFIT added quadratically to the standard deviation (6 per cent for both the Sérsic and the PSF components) of the fluxes obtained by considering different convolution box sizes in GALFIT and to the 10 per cent flux calibration uncertainty (see Table 3).

We also estimated the unresolved and integrated emission at 8.7 μm with two independent methods routinely used in the literature for ground-based mid-IR imaging. The first one is referred to as *PSF-scaling* photometry and is useful only in sources that are

dominated by the nuclear emission (see e.g. Mason et al. 2012). In this method, we measured the flux within a circular aperture of 0.5-arcsec radius. Next, we scaled the PSF-star image to the centroid of the galaxy emission and measured the flux within the same aperture around the scaled PSF star. This method provides the maximum contribution from an unresolved nuclear source. For UGC 5101, we obtained the integrated emission using a large aperture with a 9.2 arcsec radius, which is the radius at which the curve of growth flattens.

The second method we term *PSF-subtraction* (e.g. Soifer et al. 2000; Radomski et al. 2002, 2003; Levenson et al. 2009; Ramos Almeida et al. 2009, 2011; García-Bernete et al. 2014). In this method, we first matched the PSF-star image (see Fig. 1, right-hand panel) to the peak of the galaxy emission, that is, at a 100 per cent level. Then we subtracted the scaled standard PSF-star from the galaxy image at different percentage peak levels until we obtained a flat profile in the residual image at $\lesssim 0.3$ arcsec. For the CC 8.7 μm image, this was achieved at a subtraction level of 60 per cent of the peak intensity. We then measured the unresolved component by integrating the emission in a 9.2 arcsec-radius aperture on the scaled PSF-star image. We computed the integrated flux by adding the unresolved component to the extended component as measured by integrating the flux in the same aperture radius on the galaxy image after subtracting the scaled PSF image (see Fig. 1, right-hand panel).

We list in Table 3 the unresolved fluxes at 8.7 μm using the *PSF-scaling* and *PSF-subtraction* methods. We computed the uncertainties adding in quadrature the photometric error² and the uncertainty in the flux calibration (10 per cent). For the *PSF-scaling* method, we assumed a 6 per cent uncertainty due to time-variability, estimated from the variation in the signal from the standard stars, and a 13 per cent uncertainty due to PSF-variations. These uncertainties are derived in Mason et al. (2012) from several standard stars observed during the same night at mid-IR with T-ReCS and Michelle on the Gemini North telescope. The uncertainties assumed were added in quadrature to the errors previously described. For the *PSF-subtraction* method we added in quadrature, in addition to all the above error contributions, a 7 per cent of uncertainty due to ambiguity in the best subtraction of the unresolved source. The unresolved fluxes estimated with the PSF methods are in good agreement with the value estimated with GALFIT.

Table 3. Unresolved and integrated emission at 8.7 μm using three different methods.

Method	f_{unresol} (mJy)	r_{apert} (arcsec)	f_{int} (mJy)	r_{apert} (arcsec)
GALFIT	36 ± 4	9.2	205 ± 11	NA
PSF-scaling	40 ± 7	0.5	240 ± 41	9.2
PSF-subtraction	41 ± 12	9.2	168 ± 32	9.2

Notes. NA = No assigned.

² Calculated as $\sqrt{\sigma_{\text{back}}^2 N_{\text{pix}} + \sigma_{\text{back}}^2 N_{\text{pix}}^2 / N_{\text{pix-ring}}}$, where N_{pix} is the number of pixels inside the aperture considered, $N_{\text{pix-ring}}$ is the number of pixels inside a ring of 80 pixels width around the source used to estimate the background level and its standard deviation σ_{back} (Reach et al. 2005). The background in our images is completely flat, and this makes the second term of the error equation almost negligible.

In order to assess the robustness of decomposition and whether there might be a dependency with the adopted PSF, we use the acquisition image of the standard star for spectroscopy obtained 2 h after the science image (see Table 1) and repeat the calculations of `GALFIT` decomposition of UGC 5101 with this PSF model. We find an unresolved flux 27 ± 6 mJy, which is consistent with the value derived before. We also find that the Sérsic parameters are consistent with those previously derived and listed in Table 2.

We also used `GALFIT` to measure the unresolved flux in the Subaru/COMICS Q -band image at $17.7 \mu\text{m}$. In this case, we used a Gaussian profile with an FWHM $\sim 0.6\text{--}0.8$ arcsec, which is the range FWHM of the standard star (see Asmus et al. 2014), to represent the unresolved component and a Sérsic profile for the extended component. We considered three Sérsic profiles: one free, one with fixed $n = 4$, and one with fixed $n = 1$. The best fit was obtained with a FWHM = 0.65 arcsec for the unresolved component and $n = 2.1 \pm 1.8$. This produced an unresolved flux at $17.7 \mu\text{m}$ of 158 ± 32 mJy. This is lower than the unresolved flux calculated by Asmus et al. (2014) using the same data set but consistent with that in Soifer et al. (2000) using Keck imaging. The error in the unresolved emission is the quadratic sum of the standard deviation of the flux measured by fitting different profiles and the formal error from `GALFIT`.

3.2 Starburst subtracted nuclear emission from the spectroscopic data

Both the *Spitzer*/IRS and the GTC/CC spectra show emission from polycyclic aromatic hydrocarbon (PAH) features (see Figs 4 and 5; and Armus et al. 2004). This indicates the presence of a component due to star formation activity in the regions of ~ 393 pc and ~ 2.9 kpc probed by CC and IRS, respectively. In Section 4, we will also fit the starburst-subtracted nuclear GTC/CC spectrum to infer the properties of the obscuring material, presumably the dusty torus, around the AGN of UGC 5101. Before we do so, we need to remove the emission due to star formation. Spectral decomposition in the mid-IR has proven to be an efficient method to disentangle the AGN emission from that due to star formation activity in the host galaxy in luminous infrared galaxies (LIRGs), ULIRGs, AGN, and submillimetre galaxies (e.g. Pope et al. 2008; Valiante et al. 2009; Nardini et al. 2010; Mullaney et al. 2011; Alonso-Herrero et al. 2012; Ramos Almeida et al. 2014b; García-Bernete et al. 2015; Hernán-Caballero et al. 2015).

For the spectral decomposition, we used the model proposed by Pope et al. (2008). This model includes three main components: (1) a starburst dominated by the broad features due to PAH molecules up to $\sim 18 \mu\text{m}$ (Puget & Leger 1989; Allamandola, Hudgins & Sandford 1999), (2) a power-law (or warm blackbody) continuum³ that represents the obscuring material around the AGN (Genzel et al. 1998), and (3) extinction. The starburst and power-law components can be affected by different degrees of extinction, which is modelled as a foreground dust screen. The model is expressed as

$$F_\nu = c_1 \nu^{-c_2} e^{-c_3 \tau_\nu} + c_4 f_\nu(\text{PAH}) e^{-c_5 \tau_\nu}, \quad (1)$$

where τ_ν is the extinction law, c_3 and c_5 are the power-law component and starburst extinctions, c_2 is the index of the power-law,

³ Although the use of a power-law continuum in the mid-IR (up to $\lambda \sim 35 \mu\text{m}$) is not physically motivated, it represents well the AGN heated dust continuum which usually peaks at $\lambda \sim 30\text{--}50 \mu\text{m}$ (see e.g. Alonso-Herrero et al. 2011).

$f_\nu(\text{PAH})$ the starburst component, and c_1 and c_4 are the normalizing factors.

We used a total of 24 starburst galaxies from the literature including IR-bright galaxies, LIRGs, and ULIRGs (Sturm et al. 2000; Brandl et al. 2006; Rieke et al. 2009; Sargsyan et al. 2011). We used the extinction laws of Chiar & Tielens (2006) for the local interstellar medium (ISM) and the Galactic Center (GC), as they include the absorption due to silicates around 10 and $18 \mu\text{m}$. We performed a χ^2 minimization and fitted simultaneously the five free parameters c_1 , c_2 , c_3 , c_4 , and c_5 for each of the starburst templates and extinction laws.

3.2.1 Spectral decomposition of the *Spitzer*/IRS spectrum

Considering that the local ISM extinction law of Chiar & Tielens (2006) covers a range from 1.2 to $27 \mu\text{m}$ together with the high S/N and spectral range covered by the *Spitzer*/IRS spectrum 5– $35 \mu\text{m}$ compared with the GTC/CC spectrum, we started by decomposing the *Spitzer*/IRS spectrum between 5 and $26 \mu\text{m}$. Then, in Section 3.2.2, we use the starburst galaxy obtained from the best *Spitzer*/IRS spectral decomposition fit to perform the spectral decomposition of the nuclear CC spectrum. The best fit for the *Spitzer*/IRS spectrum is achieved using the LIRG ESO 244-G012 spectrum (blue line) from Sargsyan et al. (2011) and a power-law component with an index of $c_2 = 2.0 \pm 0.2$ (green line). The index of the power law is similar to that found in the mid-IR for Seyfert 1s and Seyfert 2s (Armus et al. 2007; Ramos Almeida et al. 2009, 2011; Hönig et al. 2010). The fitted power-law component in the mid-IR is consistent with the presence of a hot dust component ($T > 300$ K) found by Armus et al. (2007) for this galaxy from the fitting of the infrared spectral energy distribution (SED) of this galaxy.

We also found that the local ISM Chiar & Tielens (2006) extinction law produced a better fit to the data than GC one. As can be seen from Fig. 3, the fit reproduces well the mid-IR emission except for the bluest part of the spectrum. This is due to the presence in UGC 5101 of strong absorption due to water ice under the $6.2 \mu\text{m}$ PAH feature (see Spoon et al. 2002; Armus et al. 2004), which is not present in the extinction law. Adding the water ice absorption using the laboratory analogues of Gerakines et al. (1995) only improved marginally the fit in this spectral region and the power-law component remained the same.

Table 4 summarizes the relevant parameters of the spectral decomposition of the IRS spectrum. The errors in the derived parameters take into account the 10 per cent uncertainty assumed for the *Spitzer*/IRS spectrum and the standard deviation of the parameters by considering different initial values for the index of the power-law c_2 (see Section 3.2.2). The starburst-subtracted fluxes (observed, not corrected for extinction) at 8.7 and $12 \mu\text{m}$ (observed wavelengths) contribute proximately 54 and 50 per cent of the observed emission in the *Spitzer*/IRS spectrum, respectively. The starburst-subtracted fractional contribution at $12 \mu\text{m}$ is in agreement with that estimated by Hernán-Caballero et al. (2015) using the same IRS spectrum but an independent method. At rest-frame wavelengths longer than approximately $15 \mu\text{m}$, the power-law component appears to dominate the continuum emission in the IRS spectrum, although at $\lambda_{\text{rest}} > 35 \mu\text{m}$ the starburst component has an almost equal contribution. This is also in agreement with the 30 per cent starburst contribution found by Armus et al. (2007) for UGC 5101 using different mid-IR diagnostics.

Using the foreground extinction and silicate optical depth ratio $A_V/\tau_{\lambda,9.7} = 18$ from Roche & Aitken (1984) for the local ISM the

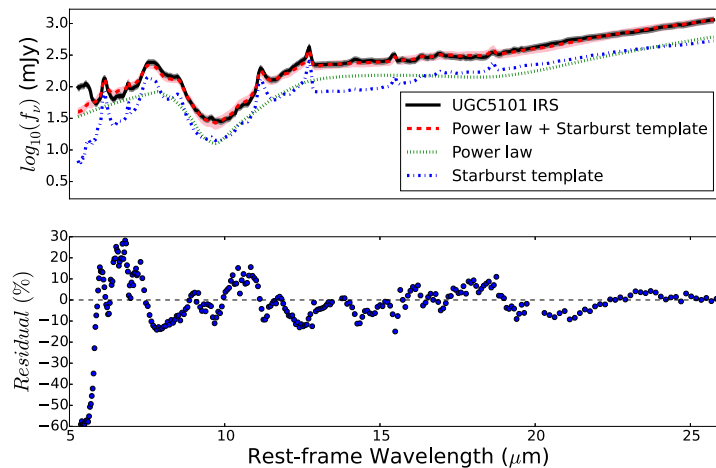


Figure 3. Upper panel: spectral decomposition of the *Spitzer*/IRS $\sim 5\text{--}35\ \mu\text{m}$ spectrum from the central 4 arcsec ($\sim 2.9\text{ kpc}$) of UGC 5101. The black line is the observed spectrum with the grey shaded region representing the 1σ uncertainty. The red line is the best-fitting model (the pink shaded area is the 1σ uncertainty of the fit), which is the sum of the fitted starburst template (blue line) and the power-law continuum component (green line). Both components are assumed to be obscured by different levels of foreground extinction using the Chiar & Tielens (2006) law for the local ISM (see the text and equation 2). Bottom panel: residuals of the fit, where percentage is defined as observed spectrum minus modelled spectrum, divided by modelled spectrum.

Table 4. Results from the spectral decomposition of the IRS and CC spectra.

Parameter	<i>Spitzer</i> /IRS	GTC/CC
Power-law index c_2	2.0 ± 0.2	2.0(fixed)
Power-law $\tau_{\lambda 9.7}$	5.1 ± 0.6	6.4 ± 2.0
Starburst $\tau_{\lambda 9.7}$	0.9 ± 0.4	0.3 ± 0.2
$8.7\ \mu\text{m } f_{\text{SBsubs}}$ (mJy)	79 ± 17	53 ± 35
$12\ \mu\text{m } f_{\text{SBsubs}}$ (mJy)	62 ± 18	42 ± 15
Reduced χ^2	2.3	3.0

Notes. f_{SBsubs} is the flux obtained from subtracting the observed spectrum and the best-fitting starburst model at 8.7 and 12 μm , respectively.

fitted foreground extinction affecting the power-law component is $A_V = 90 \pm 11\text{ mag}$, which is necessary to reproduce the deep 9.7 μm silicate feature. This high value is also consistent with the presence of dust lanes in the nuclear region, as seen in the *HST* optical image of this galaxy (Surace et al. 2000).

Finally, we note that using more typical starburst galaxy spectra, like those of Brandl et al. (2006) we obtained similar starburst-subtracted fluxes at 8.7 and 12 μm , extinctions at 9.7 μm and power-law index to those obtained with the galaxy ESO 244-G012, although the χ^2 values of the decomposition are larger.

3.2.2 Spectral decomposition of the GTC/CC spectrum

To determine the extraction type of the GTC/CC spectrum (point source versus extended source), we measured the nuclear flux on the CC 8.7 μm image within a 1 arcsec-diameter circular aperture. We obtained a flux of $57 \pm 5\text{ mJy}$ (after correction for point source emission). A comparison with the unresolved emission at 8.7 μm (Table 3) shows that for the CC slit width we can approximate the emission within the slit as a point source. For the extraction as point source, REDCAN uses an extraction aperture that increases with wavelength to account for the decreasing angular resolution. It also performs a correction to account for slit losses. We finally resampled the nuclear CC spectrum to 60 data points to improve the S/N ratio and for later fitting with CLUMPY torus models (Section 4.2). The errors are computed as the quadratic sum of the 10 per cent photometric uncertainty and the rms of the four data point rebinning.

We did the spectral decomposition of the GTC/CC nuclear spectrum as for *Spitzer*/IRS. However, because of the limited spectral range of the CC spectrum, we fixed the starburst template to the one that provided the best fit to the IRS spectrum (i.e. ESO 244-G012) and used the Chiar & Tielens (2006) extinction law of the local ISM. We found that the best fit with a reduced $\chi^2 = 2.4$ is achieved with an index of the power-law $c_2 = 4.0$. Although this value is consistent with the range of spectral indices found by Buchanan et al. (2006) in a sample of Seyfert 1, 2, LINERs and starburst galaxies, it is larger than that obtained from the *Spitzer*/IRS decomposition (see Table 4). Therefore, we study the behaviour of the c_2 index in the *Spitzer*/IRS and CC decomposition by comparing the resulting parameters when we vary c_2 between 0 and 4. From this analysis, we found that the power-law and starburst extinctions and, the starburst-subtracted fluxes at 8.7 and 12 μm are well constrained (see Table 4). Thus, we chose to fix the power-law index to $c_2 = 2.0$ for the spectral decomposition of the CC spectrum for consistency. This value agrees well with that derive from the spectral decomposition of the *Spitzer*/IRS spectrum and those measured in Seyfert 1 and 2 nuclei in the mid-IR (Hönig et al. 2010; Ramos Almeida et al. 2009, 2011).

These results are not highly dependent on the starburst template library adopted. If for instance, we fit the full spectral library of Brandl et al. (2006), we find an equally valid starburst decomposition ($\chi^2 = 3.0$) for NGC1222, and similar values for extinction, and starburst-subtracted fluxes.

We show the best-fitting model (dashed red line and shaded region) to the observed GTC/CC nuclear spectrum (black line and grey shaded region) in Fig. 4, with the green and blue lines showing the individual contributions from the power-law continuum and the starburst components, respectively. As can be seen from this figure, the best-fitting model reproduces well the data and in particular the emission of the 11.3 μm PAH feature. We therefore subtracted the starburst component from the CC spectrum, so in the next section we can model the starburst-subtracted mid-IR emission.

We list in Table 4 the relevant parameters of the fit to the CC nuclear spectrum. The errors of the parameters are estimated as the standard deviation of the parameters given by different models that fix the value of c_2 between 0 and 4. The fitted foreground extinction

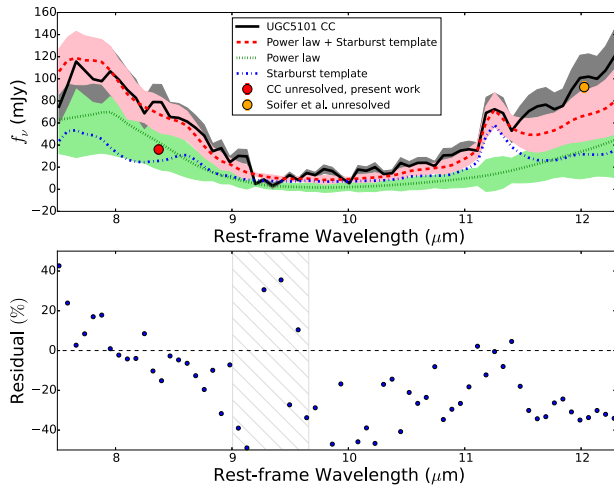


Figure 4. Upper panel: spectral decomposition of the GTC/CC nuclear (inner 393 pc) spectrum of UGC 5101. We resampled the observed spectrum to 60 data points (see the text). Lines are as in Fig. 3, where the power-law index is fixed to $c_2 = 2.0$. The filled red dot is the $8.7\ \mu\text{m}$ unresolved flux estimated from the GALFIT modelling in Section 3.1.2., whereas the orange filled dot is the $12\ \mu\text{m}$ unresolved flux from Soifer et al. (2000). Bottom panel: residuals as calculated in Fig. 3. The hatched region represents approximately the spectral range of low atmospheric transmission.

affecting the power-law continuum from the spectral decomposition of the CC nuclear spectrum $A_V = 115 \pm 36\ \text{mag}$ is higher than that from the IRS spectrum, although consistent within the uncertainties, possibly indicating that on nuclear scales the heating source is more embedded and the continuum source is extended (see below).

The starburst-subtracted fluxes, not corrected for extinction, at 8.7 and $12\ \mu\text{m}$ (observed wavelengths) from the decomposition of the CC spectrum (see Table 4) contribute approximately 67 and 59 per cent to the nuclear CC spectrum, respectively. Within the uncertainties, these values are in good agreement with those estimated by Hernán-Caballero et al. (2015) for the AGN component. The starburst-subtracted fluxes at 8.7 and $12\ \mu\text{m}$ from the *Spitzer*/IRS and CC decomposition are consistent with each other, within the uncertainties (see Table 4). In general for nearby Seyfert nuclei, the spectral decomposition of IRS spectra is able to recover both the shape and flux of the AGN component measured from high angular resolution ground-based mid-IR spectroscopy (see e.g. García-Bernete et al. 2014; Hernán-Caballero et al. 2014; Ramos Almeida et al. 2014b). In the case of UGC 5101, as it is more distant than these nearby Seyferts, it is possible that the IRS spectrum has a strong contribution from extended dust components which are more difficult to disentangle from the dust heated by the AGN.

We find, however that the $8.7\ \mu\text{m}$ starburst-subtracted nuclear flux from the decomposition of the GTC/CC nuclear spectrum is in excellent agreement to within the uncertainties with the unresolved emission derived from the GALFIT model of the CC imaging data (Section 3.1.2 and Table 3). Soifer et al. (2000) estimated that at observed $\lambda = 12.5\ \mu\text{m}$, the core component contributed approximately 50 per cent of the flux within a $4\ \text{arcsec}$ diameter aperture ($\sim 185 \pm 10\ \text{mJy}$). Within the uncertainties, their inferred unresolved flux is consistent with the starburst-subtracted GTC/CC spectrum at the same wavelength ($\sim 91\ \text{mJy}$) but not with the fitted power-law continuum (see also Fig. 5). This result shows that at this part of the spectrum, the power law is underestimated while the starburst component is well fitted.

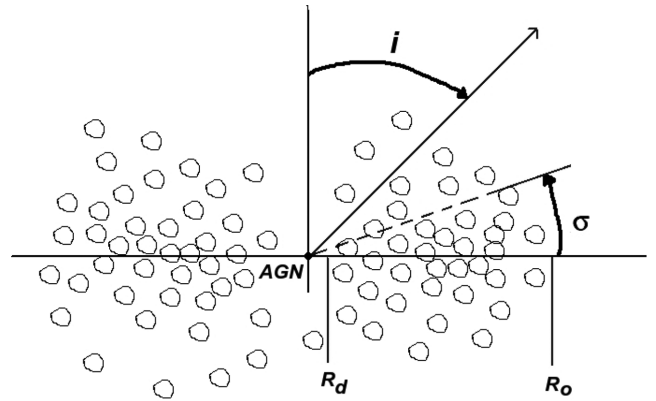


Figure 5. Cartoon showing the geometry of the CLUMPY dusty torus models of Nenkova et al. (2008a,b). According to this model, each dusty cloud has an optical depth τ_V , and the clouds are distributed between the inner radius R_d , determined by the dust sublimation temperature, and the outer radius $R_o = YR_d$, with Y a free parameter. The angular distribution of the clouds is σ . The torus viewing angle from the observer is i .

4 ESTIMATING THE PROPERTIES OF THE AGN AND THE OBSCURING MATERIAL

4.1 The CLUMPY torus models

The CLUMPY model (Nenkova, Ivezić & Elitzur 2002; Nenkova et al. 2008a,b) holds that the dust surrounding the central engine of an AGN is distributed in clumps. An illustration of this model is shown in Fig. 5. The clumps have a radial distribution $\propto r^{-q}$ with a radial extent $Y = R_o/R_d$, where R_o and R_d are the outer and inner radius of the toroidal distribution, respectively. The inner radius is defined by the dust sublimation temperature, which is assumed to be $T_{\text{sub}} \approx 1500\ \text{K}$, and the AGN luminosity as $R_d = 0.4 (1500\ \text{K } T_{\text{sub}}^{-1})^{2.6} (L_{\text{AGN}}/10^{45}\ \text{erg s}^{-1})^{0.5}\ \text{pc}$. In this model, each clump has the same optical depth (τ_V). The number of clouds along the line of sight (LOS) at a viewing angle i is $N_{\text{LOS}}(i) = N_0 e^{-(i-90)^2/\sigma_{\text{torus}}^2}$, where σ_{torus} is the angular width occupied by the cloud distribution and N_0 is the average number of clouds along a radial equatorial ray. The CLUMPY models have been proven to reproduce the nuclear IR emission of Seyfert galaxies and quasars (e.g. Mor, Netzer & Elitzur 2009; Nikutta, Elitzur & Lacy 2009; Ramos Almeida et al. 2009, 2011, 2014a,b; Alonso-Herrero et al. 2011, 2013; Lira et al. 2013; Mori et al. 2014; García-Bernete et al. 2014; Ichikawa et al. 2015; Ruschel-Dutra et al. 2014).

In this work, we use an updated version of BAYESCLUMPY, a Bayesian tool specifically designed to fit the CLUMPY models to observed SEDs and mid-IR spectroscopy (Asensio Ramos & Ramos Almeida 2009). Within BAYESCLUMPY, there are two additional parameters not listed in Table 5 that can be fitted or fixed. The first one is the scaling factor called *shift*, which accounts for the vertical displacement needed to match the fluxes of a given model to an observed SED and/or spectrum. This is proportional to the AGN bolometric luminosity. The second one is the foreground extinction A_V due to the host galaxy which is different from that produced by the torus along the LOS. We use the Chiar & Tielens (2006) extinction law derived for the local ISM, as it provided a better fit to the IRS spectrum (Section 3.2.1). Foreground extinction has been shown to be required to fit the nuclear IR emission of Seyfert nuclei with deep silicate features (see e.g. Alonso-Herrero et al. 2011; González-Martín et al. 2013), as is the case for UGC 5101. We assume a uniform prior distribution for both of them, with the

Table 5. Parameters of the CLUMPY torus models and for the best fit to nuclear emission of UGC 5101.

Parameter	Symbol	Interval	Median	MAP
Torus angular width ($^\circ$)	σ_{torus}	[15, 70]	60^{+6}_{-7}	66
Torus radial thickness	Y	[5, 100]	64^{+19}_{-23}	87
Number of clouds along an equatorial ray	N_0	[1, 15]	12^{+2}_{-3}	13
Index of the radial density profile	q	[0, 3]	$0.8^{+0.4}_{-0.4}$	1.0
Viewing angle ($^\circ$)	i	[0, 90]	55^{+18}_{-19}	46
Optical depth per single cloud	τ_V	[5, 150]	36^{+15}_{-10}	32

Notes. Columns 1, 2 and 3 show the name of the CLUMPY torus model parameters, their symbol and the fitting range. Columns 4 and 5 show the median and MAP values obtained from the posterior distributions.

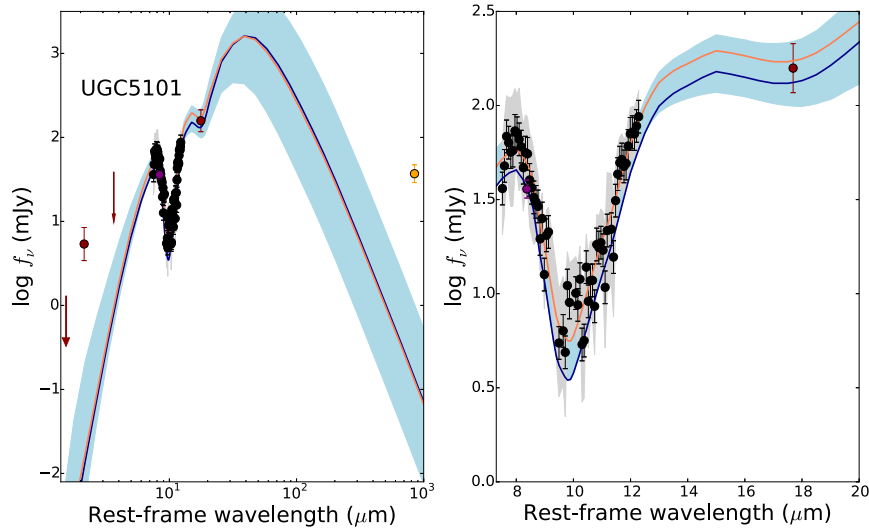


Figure 6. Left: observed unresolved nuclear SED (red dots) and mid-IR spectroscopy after subtracting the starburst contribution from the CC nuclear spectrum (black dots). The orange dot is the nuclear 880 μm continuum flux from Wilson et al. (2008). We did not use this data point for the BAYESCLUMPY fit (see the text). The blue line and shaded region represent the best CLUMPY torus model and the range of models within the 68 per cent uncertainty in the best-fitted parameters, whereas the solid orange line is the MAP model. Right: enlarged view of the best-fitting CLUMPY torus models (as in the left-hand panel) around the 9.7 and 18 μm silicate features.

foreground extinction being in the range $A_V(\text{foreground}) = 0\text{--}40$ mag. BAYESCLUMPY can also incorporate the direct AGN emission to model the data, although in principle there is no clear detection of broad emission lines in UGC 5101 (see the next section).

Under the assumption that the torus models are valid simultaneously for photometric and spectroscopic data and that the noise in all observed data is uncorrelated, the Bayesian approach is insensitive to the fact that there are many more spectroscopic points than photometric ones. This is justified by the fact that the method samples the full posterior distributions and obtains marginalized posteriors for each parameter distribution (Asensio Ramos & Ramos Almeida 2009). The results of the fitting process are the marginal posterior distributions for the six free parameters that describe the CLUMPY dusty torus model plus the vertical *shift* and foreground extinction.

4.2 Results from the fit to the unresolved SED plus the starburst-subtracted spectroscopy

We modelled the SED and spectroscopy of UGC 5101 using the near- and mid-IR unresolved fluxes plus the starburst-subtracted GTC/CC spectrum. We used as an upper limit the nuclear magnitude in the L band from Imanishi et al. (2014). Both the observed unresolved SED and GTC/CC nuclear starburst-subtracted spectrum of UGC 5101 are plotted in Fig. 6.

Table 6. Derived properties from the posterior distributions of the fitted CLUMPY torus parameters.

Parameter	Median
Extinction-corrected L_{bol} (erg s^{-1})	$(1.9^{+1.2}_{-0.7}) \times 10^{45}$
Escape probability P_{esc}	$0.0005^{+0.0040}_{-0.0005}$
Geometrical covering factor f_2	$0.94^{+0.04}_{-0.07}$
Apparent covering factor $f(i)$	$0.94^{+0.20}_{-0.15}$
Foreground extinction A_V (mag)	32^{+4}_{-7}

Notes. See equation (2) and (3) for the definition of the covering factors and escape probability.

After fitting the unresolved emission and the starburst-subtracted nuclear spectrum, we obtained the marginal posterior distributions for the six free parameters that describe the CLUMPY dusty torus model (Table 5) plus the vertical *shift* and foreground extinction A_V . If the observational data contain sufficient information for the fit, then the resulting marginal posterior distributions are centred or show trends at certain values within the considered intervals. From these posterior distributions, we also derived other torus parameters listed in Table 6.

The posterior distributions of the fitted torus model parameters show that they are well constrained (see Fig. 7 and Table 5). Both

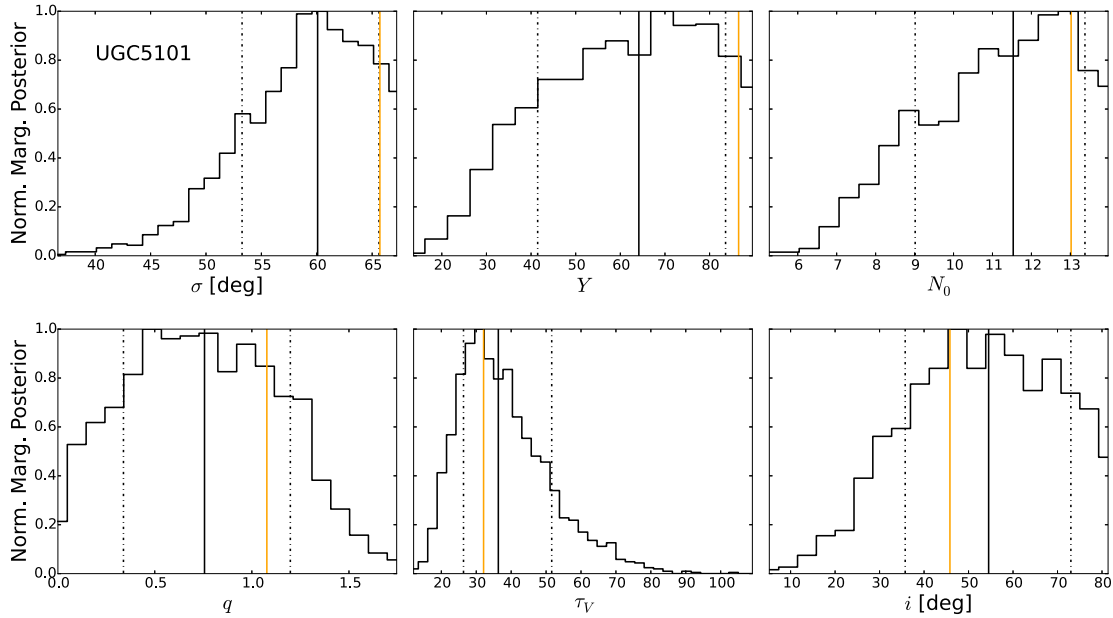


Figure 7. Marginal posterior distributions of the fitted CLUMPY torus model parameters to the nuclear emission of UGC 5101. The dotted lines represent the 1σ intervals, whereas the solid black and orange lines are the MAP and median values of the distributions, respectively.

the high value of the angular width of the torus $\sigma_{\text{torus}} \sim 60^\circ$ and number of clouds along the equatorial direction $N_0 \sim 12$ produce high apparent and geometrical covering factors $f(i) \sim 0.94$ and $f_2 \sim 0.94$, which are defined as (see Alonso-Herrero et al. 2011 for details)

$$f(i) = \frac{L_{\text{torus}}(i)}{L_{\text{bol}}^{\text{model}}(\text{AGN})} \quad (2)$$

and,

$$f_2 = 1 - \int_0^{\pi/2} P_{\text{esc}}(\beta) \cos(\beta) d\beta. \quad (3)$$

These high covering factors are consistent with the derived low escape probability for an AGN produced photon P_{esc} (see Table 6), which might explain the lack of strong AGN signatures in the optical spectrum of UGC 5101. The fitted angular size and number of clouds along the equatorial direction of the UGC 5101 torus are consistent with the values found for Seyfert 2 nuclei, whereas the torus size of UGC 5101 (~ 35 pc) is larger than the typical sizes derived for Seyfert 1 and 2 nuclei using the same modelling techniques (Alonso-Herrero et al. 2011; Ramos Almeida et al. 2011; Ichikawa et al. 2015).

The high value of the foreground extinction, $A_V = 32^{+4}_{-7}$ mag, is necessary to reproduce the deep $9.7 \mu\text{m}$ silicate feature observed in the nuclear region. However, compared with the foreground extinctions derived from the *Spitzer*/IRS and CC spectral decompositions this value is nearly three times lower. This difference can be explained considering that the CLUMPY models include the geometrical properties of the torus and, on this model, the foreground extinction is not the only contributor to the observed deep $9.7 \mu\text{m}$ silicate feature. The best-fitting models also reproduce well the $17.7 \mu\text{m}$ unresolved flux around the $18 \mu\text{m}$ silicate feature. All these values are also consistent with the parameters, including the high covering factors, derived in other LIRGs and ULIRGs hosting deeply embedded AGN, e.g. Arp 299A (Alonso-Herrero et al. 2013), NGC 6240 (Mori et al. 2014), and Mrk 1066 (Ramos Almeida et al. 2014b).

We translated the fitted torus model parameters into two model spectra. The first one corresponds to the maximum-a-posterior (MAP) values that represent the best fit to the data. The second one is produced with the median values of the probability distributions of the model parameters. We plot these best-fitting CLUMPY models in Fig. 6 together with the both unresolved SED and starburst-subtracted GTC/CC spectrum. We also show in this figure the $880 \mu\text{m}$ continuum flux of 37 ± 9 mJy measured with a $1 \text{ arcsec} \times 0.7 \text{ arcsec}$ beam (Wilson et al. 2008), although we did not use it for the fit. Clearly, the torus emission is well below this flux, indicating that in the far-IR the nuclear emission is dominated by star formation activity, as already hinted by the spectral decomposition of the IRS spectrum (Section 3.2.1). Additionally, the $880 \mu\text{m}$ flux may have a significant contribution from non-thermal or radio free-free emission (see discussion by Wilson et al. 2008).

As can be seen from Fig. 6, the best-fitting CLUMPY models reproduce well the shape of the silicate feature and the mid-IR unresolved emission. The $2.2 \mu\text{m}$ is not well fitted by the CLUMPY models. One possibility is that the near-IR unresolved emission is still contaminated by stellar emission from recent star formation in the nuclear region of the galaxy. However, in this case, the SED of the unresolved emission should be bluer than the observed nuclear $H - K = 1.9$ colour derived in this work, and at least two orders of magnitude more luminous than the AGN. Another explanation, more consistent with the nuclear $H - K$ colour, could be the presence of very hot dust clouds of graphite ($T \sim 1000$ K; see for example Mor & Trakhtenbrot 2011). In fact, Alonso-Herrero et al. (2011) found a slight excess at near-IR emission in the modelling of the SED+spectroscopy of some Seyfert 1s and, Mor et al. (2009) also consider a hot dust component for modelling the SED+spectroscopy of a sample of PG quasars.

Thus, may be in UGC 5101, a combination of CLUMPY torus emission+cold foreground absorbing dust screen might not be the appropriate model for active nuclei with very deep silicate features (e.g. Alonso-Herrero et al. 2011; Merlo et al. 2014; Mori et al. 2014) and spherically symmetric smooth models may be more appropriate

for deeply embedded objects (see Levenson et al. 2007; Alonso-Herrero et al. 2013).

4.3 The AGN luminosity

From the scaling of the fitted CLUMPY models to the data, we derived an AGN bolometric luminosity of $L_{\text{bol}} = (1.9^{+1.2}_{-0.7}) \times 10^{45} \text{ erg s}^{-1}$. Using the hard X-ray versus 12 μm correlation observed for local Seyfert galaxies (Gandhi et al. 2009; Levenson et al. 2009; Asmus et al. 2011) and the emission contribution by the starburst-subtracted nuclear component at 12 μm from the GTC/CC spectral decomposition after correcting for the derived foreground extinction (see Table 4), we predict an intrinsic hard X-ray luminosity $L_{2-10\text{keV}} = (4.1 \pm 0.7) \times 10^{43} \text{ erg s}^{-1}$. Applying a bolometric correction $[10-20] \times L_{2-10\text{keV}}$ (Marconi et al. 2004), we found a bolometric luminosity between $4.1 \times 10^{44} \leq L_{\text{bol}} \leq 8.2 \times 10^{44} \text{ erg s}^{-1}$. This range of AGN bolometric luminosities is lower than our estimate from the CLUMPY torus model fit to the unresolved nuclear IR emission and the starburst-subtracted nuclear CC spectrum of UGC 5101.

González-Martín et al. (2009) on the other hand, estimated an X-ray luminosity $L_{2-10\text{keV}} = 7 \times 10^{43} \text{ erg s}^{-1}$ after applying a Compton-thick correction to the observed 2–10 keV emission. If we consider the above bolometric correction, then the AGN bolometric luminosity is consistent with the value derived from fitting the CLUMPY torus models to the unresolved IR emission and starburst-subtracted nuclear CC spectrum with that predicted from the hard X-ray versus 12 μm correlation.

The inferred AGN bolometric luminosity from the CLUMPY torus modelling accounts approximately for ~ 56 per cent of the IR luminosity of the system, which is determined using the fluxes in all four IRAS bands (12, 25, 60 and 100 μm) and the flux–luminosity correlation in Sanders & Mirabel (1996). Considering the uncertainties in the AGN bolometric luminosity (see Table 6), this value is consistent with other estimates in the literature. For instance, Lonsdale et al. (2003) using high angular resolution radio observations estimated a 30 per cent AGN contribution in UGC 5101. Veilleux et al. (2009) derived a similar value (35 per cent) using a number of spectral mid-IR diagnostics using the *Spitzer*/IRS spectroscopy.

In summary, despite the fact that the CLUMPY models do not fit simultaneously all the near- and mid-IR unresolved emission, and starburst-subtracted nuclear CC spectrum of UGC 5101, the derived AGN bolometric luminosity is consistent with estimates using other methods. In our modelling, the AGN bolometric luminosity is only a function of the scaling factor of the models to the data, which is driven mostly by the fluxes near the peak of the torus emission. In the case of UGC 5101, the peak of the best-fitting CLUMPY torus model is at $\lambda_{\text{rest}} \sim 40\text{--}50 \mu\text{m}$ (see Fig. 6, left-hand panel) and the *Q*-band data point (observed 17.7 μm) is the closest to that peak. Therefore even for deeply embedded AGN, the modelling of the unresolved nuclear emission and the starburst-subtracted spectroscopy with the CLUMPY torus models can still be useful for deriving the AGN bolometric luminosity, as this quantity is driven by the scaling of the model and is less subject to the detailed modelling of the near and mid-IR SED and the silicate feature.

5 SUMMARY AND CONCLUSIONS

We have presented new high angular resolution (0.3–0.4 arcsec) 8.7 μm mid-IR imaging and 7.5–13 μm spectroscopy of the nuclear region of the ULIRG UGC 5101 using CC on the GTC. We

also analysed archival *HST*/NICMOS near-IR and Subaru/COMICS *Q*-band imaging and *Spitzer*/IRS spectroscopy. The presence of PAH emission in the nuclear (central $\sim 393 \text{ pc}$) CC spectrum indicates that some of the dust in central region is being heated by the UV radiation of relatively young stars. Therefore, to study the physical and geometrical properties of the obscuring material surrounding the AGN of UGC 5101, it was necessary to disentangle the IR emission presumably due to dust heated by the AGN from that due to nuclear star formation and/or stellar emission.

By using GALFIT, we were able to separate the unresolved nuclear emission from the extended host galaxy emission using the near-IR (1.60 and 2.22 μm) and mid-IR (8.7 and 17.7 μm) imaging data. We also calculated the unresolved emission at 8.7 μm with other methods, namely *PSF-subtraction* and *PSF-scaling* and found that the resulting fluxes were similar to those derived with GALFIT. In addition, we found that the Sérsic parameters, which represent the extended emission, derived at near- and mid-IR wavelengths are consistent with each other.

For the mid-IR spectroscopy, we used a spectral decomposition method to estimate the emission of the obscuring material around the AGN, which we represented as an extinguished power-law continuum. We also allowed both components to have different foreground extinctions. From the spectral decomposition of the IRS data, we found an index of the power law ($c_2 = 2.0 \pm 0.2$) consistent with the values observed for Seyfert 1 and Seyfert 2 nuclei (Ramos Almeida et al. 2011). Given the limited spectral range of the CC spectrum for the decomposition, we fixed the index of the power law and starburst template to those derived for the IRS data. Within the uncertainties, the starburst-subtracted nuclear fluxes at 8.7 and 12 μm CC continuum component are consistent with those derived from the spectral decomposition of the IRS spectrum. In addition, the starburst-subtracted nuclear flux at 8.7 μm is also consistent within the uncertainties with the value derived with the GALFIT modelling of the CC imaging data. We also estimated that in the central 393 pc of UGC 5101 the power-law component at 8.7 and 12 μm (observed wavelengths) contributes 67 and 59 per cent of the nuclear emission, respectively.

Before fitting the unresolved SED of UGC 5101 with the CLUMPY torus models of Nenkova et al. (2008a,b), we subtracted the fitted starburst component from the GTC/CC nuclear observed spectrum. We found that CLUMPY torus models with a high covering factor and a high foreground extinction ($A_V \sim 32 \text{ mag}$) fit well the silicate feature and unresolved mid-IR emission. The high value of the foreground extinction is similar to results for other deeply embedded AGN in local LIRGs and ULIRGs (see e.g. Alonso-Herrero et al. 2013; Mori et al. 2014). However, the observed unresolved near-IR emission of UGC 5101 is well above the fitted CLUMPY models. This could be due to contamination by nuclear stellar emission even at the angular resolution of 0.15 arcsec of the NICMOS data or more likely due to the presence of hot dust clouds. We also showed that the observed 880 μm nuclear flux is much higher than the extrapolation to the far-IR of the fitted torus models. Again, this indicates that there is strong nuclear star formation, as also indicated by the presence of PAH emission in the CC spectrum, and this component also dominates the far-IR nuclear emission of UGC 5101.

Even though the CLUMPY torus models are not able to reproduce simultaneously the nuclear unresolved near and mid-IR emission, and the starburst-subtracted GTC/CC nuclear spectrum of UGC 5101, the derived AGN bolometric luminosity ($L_{\text{bol}} \sim 1.9 \times 10^{45} \text{ erg s}^{-1}$) is consistent with that estimated from hard X-rays

(González-Martín et al. 2009) but higher than that from the 2–10 keV versus 12 μ m correlation (Gandhi et al. 2009; Levenson et al. 2009; Asmus et al. 2011).

ACKNOWLEDGEMENT

We thank the referee for a thorough report that has improved the paper significantly. This work has been partly supported by Mexican CONACyT under research grant CB-2011-01-167291. MM-P acknowledges support by the CONACyT PhD fellowship programme. AA-H and AH-C acknowledge financial support from the Spanish Plan Nacional de Astronomía y Astrofísica under grant AYA2012-31447, which is partly funded by the FEDER programme, and the Universidad de Cantabria through the Augusto G. Linares programme. CRA is supported by a Marie Curie Intra European Fellowship within the 7th European Community Framework Programme (PIEF-GA-2012-327934). IG-B acknowledges financial support from the Instituto de Astrofísica de Canarias through Fundación La Caixa and from the Spanish Ministry of Science and Innovation (MICINN) through project PN AYA2013-47742-c4-2-P (Estallidos).

This work is based on observations made with the GTC, installed in the Spanish Observatorio del Roque de los Muchachos of the Instituto de Astrofísica de Canarias, in the island of La Palma. It is also based partly on observations obtained with the Spitzer Space Observatory, which is operated by JPL, Caltech, under NASA contract 1407. This research has made use of the NASA/IPAC Extragalactic Database (NED) which is operated by JPL, Caltech, under contract with the National Aeronautics and Space Administration. The CASSIS is a product of the Infrared Science Center at Cornell University, supported by NASA and JPL. Based on observations made with the NASA/ESA *HST*, obtained from the data archive at the Space Telescope Science Institute. STScI is operated by the Association of Universities for Research in Astronomy, Inc. under NASA contract NAS 5-26555.

REFERENCES

- Allamandola L. J., Huggins D. M., Sandford S. A., 1999, *ApJ*, 511, L115
 Alonso-Herrero A., Quillen A. C., Simpson C., Efstathiou A., Ward M. J., 2001, *AJ*, 121, 1369
 Alonso-Herrero A. et al., 2011, *ApJ*, 736, 82
 Alonso-Herrero A., Pereira-Santaella M., Rieke G. H., Rigopoulou D., 2012, *ApJ*, 744, 2
 Alonso-Herrero A. et al., 2013, *ApJ*, 779, L14
 Armus L. et al., 2004, *ApJS*, 154, 178
 Armus L. et al., 2007, *ApJ*, 656, 148
 Asensio Ramos A., Ramos Almeida C., 2009, *ApJ*, 696, 2075
 Asmus D., Gandhi P., Smette A., Hönig S. F., Duschl W. J., 2011, *A&A*, 536, AA36
 Asmus D., Hönig S. F., Gandhi P., Smette A., Duschl W. J., 2014, *MNRAS*, 439, 1648
 Brandl B. R. et al., 2006, *ApJ*, 653, 1129
 Buchanan C. L., Kastner J. H., Forrest W. J., Hrivnak B. J., Sahai R., Egan M., Frank A., Barnbaum C., 2006, *AJ*, 132, 1890
 Chiar J. E., Tielens A. G. G. M., 2006, *ApJ*, 637, 774
 Cohen J. G., 1999, *AJ*, 117, 2428
 Downes D., Solomon P. M., 1998, *ApJ*, 507, 615
 Gandhi P., Horst H., Smette A., Hönig S., Comastri A., Gilli R., Vignali C., Duschl W., 2009, *A&A*, 502, 457
 García-Bernete I. et al., 2015, *MNRAS*, 449, 1309
 Genzel R. et al., 1998, *ApJ*, 498, 579
 Gerakines P. A., Schutte W. A., Greenberg J. M., van Dishoeck E. F., 1995, *A&A*, 296, 810
 González-Martín O., Masegosa J., Márquez I., Guainazzi M., 2009, *ApJ*, 704, 1570
 González-Martín O. et al., 2013, *A&A*, 553, AA35
 Haan S. et al., 2011, *AJ*, 141, 100
 Hernán-Caballero A. et al., 2015, *ApJ*, 803, 109
 Hönig S. F., Kishimoto M., Gandhi P., Smette A., Asmus D., Duschl W., Polletta M., Weigelt G., 2010, *A&A*, 515, AA23
 Houck J. R. et al., 2004, *ApJS*, 154, 211
 Ichikawa K. et al., 2015, *ApJ*, 803, 57
 Imanishi M., Saito Y., 2014, *ApJ*, 780, 106
 Imanishi M., Dudley C. C., Maloney P. R., 2001, *ApJ*, 558, L93
 Imanishi M., Terashima Y., Anabuki N., Nakagawa T., 2003, *ApJ*, 596, L167
 Kim D.-C., 1995, PhD thesis, Univ. Hawaii
 Kormendy J., Sanders D. B., 1992, *ApJ*, 390, L53
 Krist J., 1993, in Hanisch R. J., Brissenden R. J. V., Barnes J., eds, *ASP Conf. Ser. Vol. 52, Astronomical Data Analysis Software and Systems II*. Astron. Soc. Pac., San Francisco, p. 536
 Leboutteiller V., Barry D. J., Spoon H. W. W., Bernard-Salas J., Sloan G. C., Houck J. R., Weedman D. W., 2011, *ApJS*, 196, 8
 Levenson N. A., Sirocky M. M., Hao L., Spoon H. W. W., Marshall J. A., Elitzur M., Houck J. R., 2007, *ApJ*, 654, L45
 Levenson N. A., Radomski J. T., Packham C., Mason R. E., Schaefer J. J., Telesco C. M., 2009, *ApJ*, 703, 390
 Lira P., Videla L., Wu Y., Alonso-Herrero A., Alexander D. M., Ward M., 2013, *ApJ*, 764, 159
 Lonsdale C. J., Smith H. E., Lonsdale C. J., 1995, *ApJ*, 438, 632
 Lonsdale C. J., Lonsdale C. J., Smith H. E., Diamond P. J., 2003, *ApJ*, 592, 804
 Marconi A., Risaliti G., Gilli R., Hunt L. K., Maiolino R., Salvati M., 2004, *MNRAS*, 351, 169
 Mason R. E. et al., 2012, *AJ*, 144, 11
 Medling A. M. et al., 2014, *ApJ*, 784, 70
 Merlo M. J. et al., 2014, *ApJ*, 788, 6
 Mor R., Trakhtenbrot B., 2011, *ApJ*, 737, L36
 Mor R., Netzer H., Elitzur M., 2009, *ApJ*, 705, 298
 Mori T. I. et al., 2014, *PASJ*, 66, 93
 Mullane J. R., Alexander D. M., Goulding A. D., Hickox R. C., 2011, *MNRAS*, 414, 1082
 Nardini E., Risaliti G., Watabe Y., Salvati M., Sani E., 2010, *MNRAS*, 405, 2505
 Nenkova M., Ivezić Ž., Elitzur M., 2002, *ApJ*, 570, L9
 Nenkova M., Sirocky M. M., Ivezić Ž., Elitzur M., 2008a, *ApJ*, 685, 147
 Nenkova M., Sirocky M. M., Nikutta R., Ivezić Ž., Elitzur M., 2008b, *ApJ*, 685, 160
 Nikutta R., Elitzur M., Lacy M., 2009, *ApJ*, 707, 1550
 Packham C., Telesco C. M., Hough J. H., Ftaclas C., 2005, *Rev. Mex. Astron. Astrofis. Ser. Conf.*, 24, 7
 Peng C. Y., Ho L. C., Impey C. D., Rix H.-W., 2002, *AJ*, 124, 266
 Pope A. et al., 2008, *ApJ*, 689, 127
 Ptak A., Heckman T., Levenson N. A., Weaver K., Strickland D., 2003, *ApJ*, 592, 782
 Puget J. L., Leger A., 1989, *ARA&A*, 27, 161
 Radomski J. T., Piña R. K., Packham C., Telesco C. M., Tadhunter C. N., 2002, *ApJ*, 566, 675
 Radomski J. T., Piña R. K., Packham C., Telesco C. M., De Buizer J. M., Fisher R. S., Robinson A., 2003, *ApJ*, 587, 117
 Ramos Almeida C. et al., 2009, *ApJ*, 702, 1127
 Ramos Almeida C. et al., 2011, *ApJ*, 731, 92
 Ramos Almeida C., Alonso-Herrero A., Levenson N. A., Asensio Ramos A., Rodríguez Espinosa J. M., González-Martín O., Packham C., Martínez M., 2014a, *MNRAS*, 439, 3847
 Ramos Almeida C. et al., 2014b, *MNRAS*, 445, 1130
 Reach W. T. et al., 2005, *PASP*, 117, 978
 Rieke G. H., Alonso-Herrero A., Weiner B. J., Pérez-González P. G., Blaylock M., Donley J. L., Marcillac D., 2009, *ApJ*, 692, 556
 Roche P. F., Aitken D. K., 1984, *MNRAS*, 208, 481

- Ruschel-Dutra D., Pastoriza M., Riffel R., Sales D. A., Winge C., 2014, MNRAS, 438, 3434
- Sanders D. B., Mirabel I. F., 1996, ARA&A, 34, 749
- Sanders D. B., Soifer B. T., Elias J. H., Madore B. F., Matthews K., Neugebauer G., Scoville N. Z., 1988a, ApJ, 325, 74
- Sanders D. B., Soifer B. T., Elias J. H., Neugebauer G., Matthews K., 1988b, ApJ, 328, L35
- Sargsyan L., Weedman D., Lebouteiller V., Houck J., Barry D., Hovhannisyan A., Mickaelian A., 2011, ApJ, 730, 19
- Scoville N. Z. et al., 2000, AJ, 119, 991
- Soifer B. T. et al., 2000, AJ, 119, 509
- Spoon H. W. W., Keane J. V., Tielens A. G. G. M., Lutz D., Moorwood A. F. M., Laurent O., 2002, A&A, 385, 1022
- Stierwalt S. et al., 2013, ApJS, 206, 1
- Sturm E., Lutz D., Tran D., Feuchtgruber H., Genzel R., Kunze D., Moorwood A. F. M., Thornley M. D., 2000, A&A, 358, 481
- Surace J. A., Sanders D. B., Evans A. S., 2000, ApJ, 529, 170
- Telesco C. M. et al., 2003, in Iye M., Moorwood A. F. M., eds, Proc. SPIEConf. Ser. Vol. 4841, Instrument Design and Performance for Optical/Infrared Ground-based Telescopes. SPIE, Bellingham, p. 913
- Thompson R. I., Storrie-Lombardi L. J., Weymann R. J., Rieke M. J., Schneider G., Stobie E., Lytle D., 1998, preprint ([astro-ph/9810285](https://arxiv.org/abs/astro-ph/9810285))
- Valiante E., Lutz D., Sturm E., Genzel R., Chapin E. L., 2009, ApJ, 701, 1814
- Veilleux S., Kim D.-C., Sanders D. B., Mazzarella J. M., Soifer B. T., 1995, ApJS, 98, 171
- Veilleux S. et al., 2009, ApJS, 182, 628
- Wilson C. D. et al., 2008, ApJS, 178, 189
- Yuan T.-T., Kewley L. J., Sanders D. B., 2010, ApJ, 709, 884

This paper has been typeset from a \LaTeX file prepared by the author.